npj computational materials

www.nature.com/npjcompumats

ARTICLE OPEN

Check for updates

Electric-controlled tunable thermal switch based on Janus monolayer MoSSe

Donghai Wei[1], E Zhou[1], Xiong Zheng[1], Huimin Wang[2]✉, Chen Shen[3]✉, Hongbin Zhang[3], Zhenzhen Qin[4]✉ and Guangzhao Qin[1]✉

The high-performance, wide-range tunable thermal switches play a significant role in the thermal management, high-power-density intelligent devices, energy systems, etc. However, traditional thermal switch components, such as thermal diodes, suffer from poor stability, small adjustability, low time efficiency, and difficult implementation. Herein, we propose the superior electric-controlled thermal switch (ECTS) based on Janus monolayer MoSSe. The high-effective and asymmetric regulation of the thermal conductivity driven by electric field demonstrates a wide-range adjustable thermal switch ratio, where the peak value reaches 2.09 under the electric field of 0.04 VÅ^{-1}. The underlying mechanism is revealed by electronic structures that the interactions between electrons and phonons are renormalized due to the electric field driving charge density redistribution, which ultimately modulates the phonon anharmonicity. The high-efficiency adjustable ECTS component is expected to provide new inspiration for next-generation thermal management and information processing.

npj Computational Materials (2022)8:260 ; https://doi.org/10.1038/s41524-022-00944-y

INTRODUCTION

Dynamically regulating phonon transport properties plays a significant role in high-performance thermal management[1–3], energy system[4–6], intellectual terminal and space technology[7,8]. To date, large temperature fluctuations (extremely high or low) are still one of the most critical factors restricting the stability of chip performance. For instance, electric vehicle, as the necessary means of transportation, suffers from the challenges of cold climate or regions, and the performance is limited by the battery thermal management system[9–12]. Thus, developing high-efficiency and adjustable thermal switches has become increasingly urgent and important.

With different regulatory effects on thermal conductance or conductivity, previous reports mainly focus on thermal switches, thermal diodes, and other heat-related components[8]. As an analogue of electrical switch, thermal switch realizes the thermal modulation by regulating the thermal conductance or conductivity between the "on" and "off" states[13]. The switch ratio *r*, which demonstrate the merit of the thermal switch component, is defined as

$$r = \frac{G_{on}}{G_{off}} = \frac{q_{on}/\Delta T_{on}}{q_{off}/\Delta T_{off}} \quad (1)$$

where the *G* is the thermal conductance or conductivity, and the *q* and ΔT are the heat flow and the temperature difference, respectively, under the different "on" and "off" states. Varieties of traditional thermal switches are realized by the different physical mechanism, which can be divided into gas-based thermal switches[14–16], fluid-based thermal switches[17–19], as well as phase-change-based solid-state thermal switches[20–24]. For instance, Vanapalli et al. reported the gas-gap thermal switch (H_2 and He) at cryogenic temperature about 120 K, where the *r* reached 35 and 37 for the different H_2 and He gases, respectively[15]. In addition, a liquid metal droplet (Galinstan) thermal switch was studied by Yang et al., where the *r* was greater than 70 at heat fluxes near 10 W/cm^2[17]. Moreover, the phase-change thermal switches also play a key role in the thermal switch family. Shrestha et al. reported a high-contrast reversible thermal regulator driven by the structural phase transition in crystalline polyethylene with a ~10× thermal switching ratio[20]. Besides, the mechanisms have been also widely studied for the thermal switching modulation based on metal-insulator transitions[25], solid-liquid phase transitions[8], electrochemical method[26], etc. Most recently, the compressible graphene composite foams are designed for the tunable thermal switching with a large *r* (~8×)[27]. Nevertheless, the lifetime is undoubtedly a concern for strain-driven thermal switches. In fact, all the solid-state thermal switches, more or less, suffer from the disadvantages of poor stability, weak adjustability, and low time efficiency[28,29].

In addition to the regulation manners as mentioned above, external electric field plays a key role in regulating the physical properties of materials[30–38], which has been widely studied for manipulating thermal transport. For instance, Qin et al. obtained the largely modulated thermal conductivity of silicene, which reaches two orders of magnitude lowered thermal conductivity compared to the pristine state by applying an *out-of-plane* external electrical field of 0.5 VÅ^{-1}[39]. Following the same strategy, Yang et al. realized the transition of thermal conductivity from anisotropy to isotropy for monolayer borophene[40]. As an excellent reversible non-destructive thermal transport regulation method, electric field has great potential to be used for realizing thermal switches, which has been verified in the fluid-based thermal diodes[41,42]. However, researches on the solid-state thermal switches driven by the electric field are rare, and are mainly limited in ferroelectric materials[43–45], where the "on" and "off" states

[1]State Key Laboratory of Advanced Design and Manufacturing for Vehicle Body, College of Mechanical and Vehicle Engineering, Hunan University, 410082 Changsha, P. R. China. [2]Hunan Key Laboratory for Micro-Nano Energy Materials & Device and School of Physics and Optoelectronics, Xiangtan University, 411105 Xiangtan, Hunan, China. [3]Institute of Materials Science, Technical University of Darmstadt, Alarich-Weiss-Str. 2, 64287 Darmstadt, Germany. [4]School of Physics and Microelectronics, Zhengzhou University, 450001 Zhengzhou, China. ✉email: wanghmin@xtu.edu.cn; chenshen@tmm.tu-darmstadt.de; qzz@zzu.edu.cn; gzqin@hnu.edu.cn

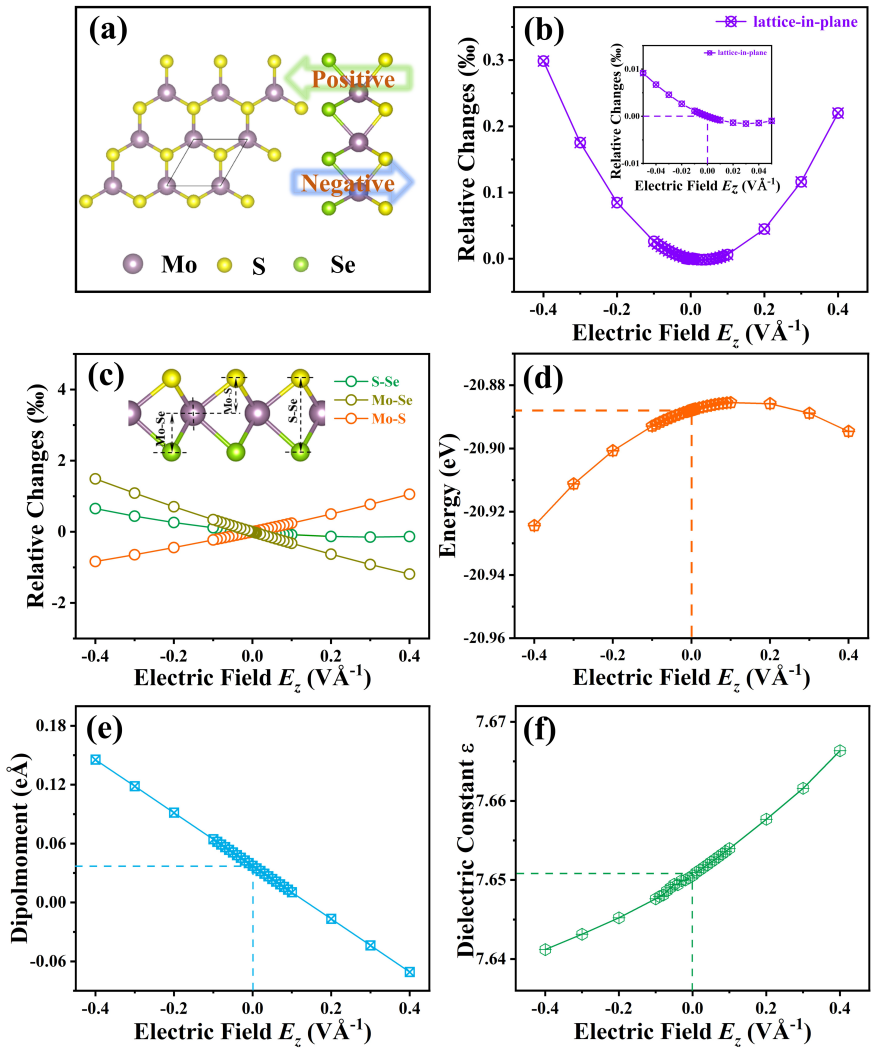

Fig. 1 The effect of electric field on MoSSe. a The top and side views of the configuration of 2H MoSSe. The primitive cell is marked by the gray line. The Mo, S, and Se atoms are plotted as the purple, yellow, and green balls. The arrows indicate the directions of the external electric fields, where positive refers to the vertical direction from the S to Se atom planes and negative refers to the reversed direction. **b** The variation of the *in-plane* lattice constants under the electric fields ranging from −0.4 to 0.4 VÅ^{-1}. (Inset) The enlarged view for the electric fields ranging from −0.05 to +0.05 VÅ^{-1}. **c** The relative distance changes of the S-Se, Mo-Se, and Mo-S atoms planes. The **d** energy, **e** dipole moment, and **f** dielectric constant as a function of the external electric field.

can be realized by the different ferroelectric domain walls response. Consequently, it is of great significance to develop new reversible solid-state-based thermal switches realized by applying electric field.

In this work, we systematically studied the thermal transport properties of Janus monolayer MoSSe with external electric field applied. It is shown that the thermal transport in Janus monolayer MoSSe exhibits significant adjustability that the thermal conductivity reaches 2.13 times the pristine value under an electric field of 0.040 VÅ^{-1} applied from S to Se atom. In contrast, the effect of the opposite electric field (from Se to S atom) is almost negligible. The significant difference in thermal transport response to the electric field along different directions can be used to manufacture electric-controlled thermal switch (ECTS), which is mainly attributed to the intrinsic *out-of-plane* asymmetry of Janus monolayers MoSSe. The success in realizing ECTS from differentiated modulation effect by the asymmetric structural engineering not only expand the design capabilities of thermal switches, but also provide an efficient thermal management solution, which can be used in electric vehicle and intelligent terminal, etc.

RESULTS

Electric field response of Janus MoSSe structure

The sandwich-like structure of 2H phase Janus monolayer MoSSe is shown in Fig. 1a. Different from the monolayer MoS_2 or $MoSe_2$, the Janus monolayer MoSSe possesses three atomic sublayers constructed by replacing a layer of S (Se) atom with Se (S) atoms in the MoS_2 ($MoSe_2$) monolayer. Thus, the reflection symmetry is broken compared with the MoS_2($MoSe_2$). In addition, the distances of the Mo-S and Mo-Se planes are different, which is caused by the different electronegativity of S (2.58) and Se (2.55) and also the different atomic radius. As a result, spontaneous polarization can be observed along the *out-of-plane* direction. Moreover, the optimized *in-plane* lattice constant is 3.25 Å for Janus monolayer MoSSe. The $d_{Mo\text{-}S}$ (distance of the Mo-S plane), $d_{Mo\text{-}Se}$ (distance of the Mo-Se plane), and $d_{S\text{-}Se}$ (distance of the S–Se plane) are 1.52, 1.71, and 3.23 Å, respectively. The bond lengths of Mo–S and Mo–Se are 2.42 and 2.54 Å, respectively. The geometry parameters as obtained in this study are well consistent with previous reports[46].

The external electric fields are applied perpendicular to the MoSSe monolayer, *i.e.*, along the *out-of-plane* directions as shown

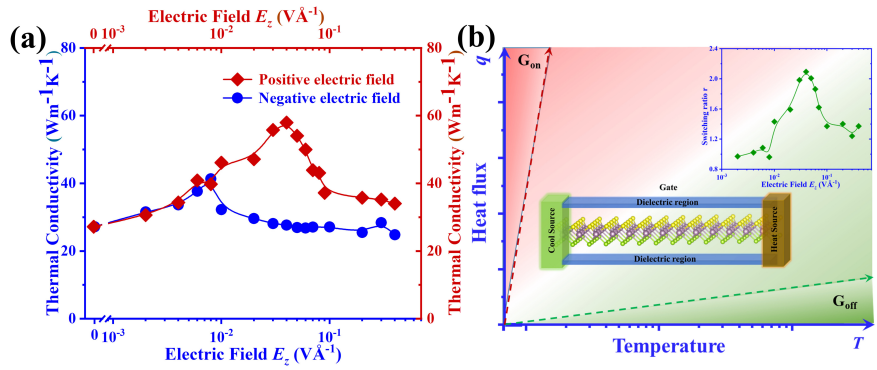

Fig. 2 The asymmetric behavior of thermal transport modulated by electric field. a The thermal conductivity at 300 K under the positive and negative external electric fields ranging from 0 to 0.4 VÅ^{-1}. **b** The schematic diagram for the ECTS (Inset: the tunable switching ratio as a function of external electric fields).

in Fig. 1a. From the geometry evolution of MoSSe under electric field as shown in the Fig. 1b, c, it is interesting to find that, with the increasing electric fields, the *in-plane* lattice constant increases whether positive or negative external electric fields are applied. It is strikingly different from the change of monolayer thickness (distance of the S-Se atom plane), where the increasing phenomenon only happens when negative electric fields are applied. Thus, the negative Poisson's ratio occurs in monolayer MoSSe when the external electric field is applied from the Se to S atom planes. Moreover, the lattice constants change asymmetrically when electric fields are applied along different directions as mentioned above (the difference can reach 0.078‰ under electric field of 0.4 VÅ^{-1}). Such asymmetry is also reflected in the ground state energy shown in Fig. 1d.

The decreased energy implies the enhanced stability of the Janus monolayer MoSSe under external electric fields. The dipole moment decreases linearly as the electric field increases (Fig. 1e), while the dielectric constant increases monotonically with the increasing electric fields, as shown in Fig. 1f. It is worth noting that the dipole moments and the dielectric constants are 0.037 eÅ and 7.650 without electric field, respectively. The intrinsic dipole moment and the dielectric constant can be attributed to the asymmetry of the structure. The intrinsic vertical piezoelectric response and vertical dipoles have also been well verified in previous studies[47,48]. Due to the structural asymmetry, the lattice constant, thickness, and energy show asymmetrical changes under the same intensity of positive and negative electric fields.

The dynamical stability is further verified by the phonon dispersions without any imaginary frequencies under the representative electric fields together with the unapplied electric field as described in Supplementary Fig. 1. No appreciable changes can be found for the low-frequency acoustic phonons, while slight changes occur for high-frequency optical phonons under positive or negative electric fields compared with the pristine state. The slightly changed phonon dispersions implies that the external electric field has a neglected effect on the phonon group velocity, as shown in Supplementary Figs. 4a, 5a.

Tunable switching effect

The modulated thermal conductivity at 300 K under the positive and negative external electric fields ranging from 0 to 0.4 VÅ^{-1} is shown in Fig. 2a. To ensure the accuracy of the calculated thermal conductivity, the convergence test of cutoff radius and *Q*-grid for Janus MoSSe without electric field are fully carried out as shown in Supplementary Fig. 2. The results demonstrate that the thermal conductivity is well converged at the cutoff radius including seventh-nearest neighbors as well as the 101 × 101 × 1 *Q*-grids. In view of the convergence test and the consistent results, the same cutoff radius and *Q*-grids setting are used for all the following calculations.

Under the positive electric fields, the thermal conductivity increases first with the increasing electric field strength, and then decreases monotonously after reaching the peak value at $E_z = 0.04$ VÅ^{-1}. As a result, the modulated thermal conductivity of the Janus MoSSe reaches 2.09 times that with reversed electric fields applied. Such a selective regulation driven by the external electric field based on the asymmetric structure of MoSSe finally realizes the switching effect, which is confirmed in Fig. 2b.

Commonly, the traditional thermal switches only demonstrate the "on" and "off" states (G_{on} and G_{off} demonstrated in Fig. 2b by the dot dash line) with the absence of the adjustability. Here, the thermal switch driven by the external electric field not only realize the wide-range adjustability but also possess high time efficiency. The large switch ratio in the ECTS can reach 2.09 under the electric field of 0.04 VÅ^{-1}.

In fact, the behavior of on/off switch and the wide-range adjustability in the ECTS is somehow similar to the field effect transistor (FET) with two important functions of switch and current change amplifier. Compared to FET, the ECTS that can also be called as the electric-controlled thermal transistor (ECTT) has three poles, which can be defined as Drain, Source, and Gate, respectively. The difference is that the electric fields applied in ECTS change the heat flow rather than the current in FET. As demonstrated in Supplementary Fig. 3, the normalized heat currents J_D/J_S is a function of the voltage applied on the Gate. The thermal transport properties can be regulated when the external electric fields are applied in either direction perpendicular to the monolayers. The differentiated modulation driven by the external electric fields functionalizes the ECTS. Thus, the heat flux from heat to cold end can be enhanced in the "on" state by applying a positive voltage on the gate, while the negative voltage keeps the ECTS in the "off" state.

Mode level analysis

To study the differentiated modulation mechanism demonstrated by bidirectional electric fields on the thermal transport properties of Janus monolayer MoSSe, the comparative analysis of the scattering rate and the Grüneisen parameter is presented in Fig. 3. The apparent decrease of the scattering rate can be seen under the positive electric field of 0.04 VÅ^{-1}, while there are only slight changes for the negative electric fields. The low scattering rate suggests a long phonon lifetime and further a high thermal conductivity. As it is well known that the scattering rate mainly depends on the scattering strength and channels, which are quantified by the Grüneisen parameter and volume in phase space[49,50] (more details are shown in Supplementary Fig. 4b, 5b), respectively. The similar order of magnitude in phase space drives us to explore the phonon anharmonicity expressed by the Grüneisen parameter shown in Fig. 3c, d. Widely spreading that the smaller the absolute value of the Grüneisen parameter, the weaker anharmonicity among phonons.

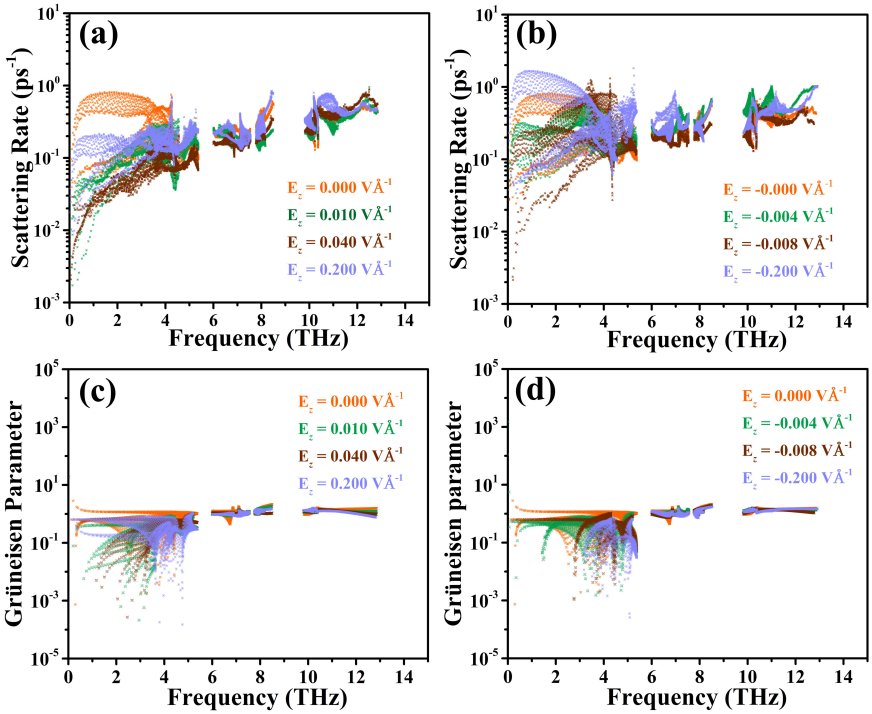

Fig. 3 The comparison of scattering rate and Grüneisen parameter under different external electric fields. a, **c** For positive electric fields. **b**, **d** For negative electric fields.

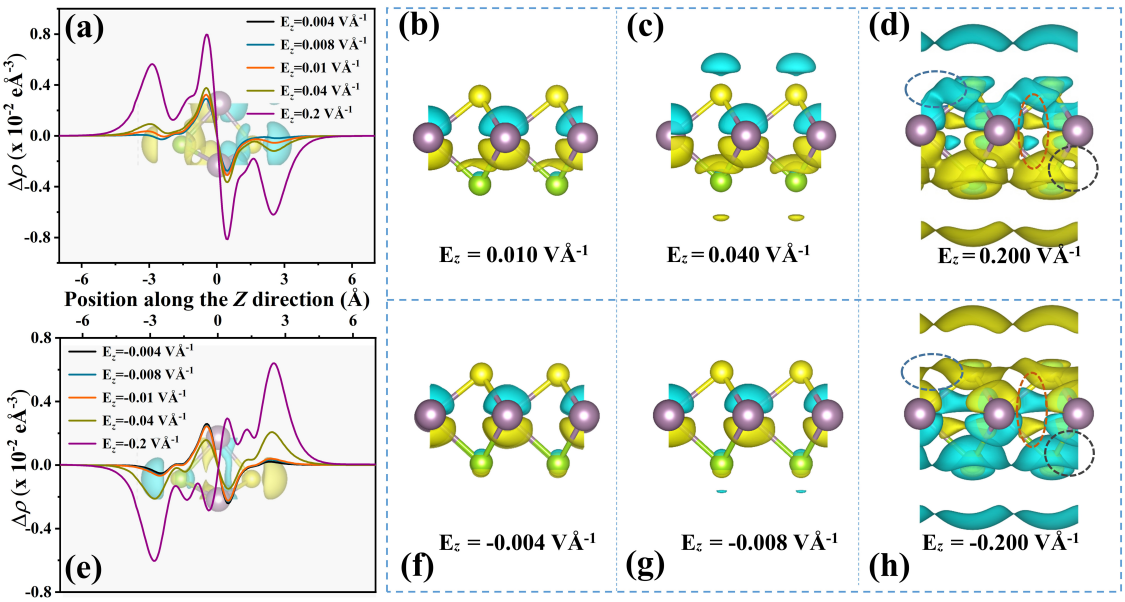

Fig. 4 The difference in charge density induced by the representative positive **a** and negative **e** electric fields. The detailed analysis is presented based on the representative electric fields of 0.010 **b**, 0.040 **c**, and 0.200 VÅ^{-1} **d**, as well as −0.004 **f**, −0.008 **g**, and −0.200 VÅ^{-1} **h** ($\Delta\rho = \rho(E_z) - \rho(E_z = 0)$) (yellow: positive accumulation of charge, blue: negative depletion of charge). The isosurface is 10^{-5} for the contour plot.

Because the low-frequency phonon branches dominate the contribution to the thermal conductivity, the statistical data of the Grüneisen parameter is calculated for the frequency region below 5.8 THz. The absolute value of the sum of the Grüneisen parameter under the positive (negative) electric fields are 1205.3, 1088.4, 1030.2, 1627.8 (1205.3, 545.2, 176.8, 1088.3), respectively, corresponding to the electric field intensity of 0.000, 0.010, 0.040, and 0.200 VÅ^{-1}, respectively. The statistical results agree well with the variation trend of the thermal conductivities under the external electric fields.

Difference in charge density induced by electric fields

Furthermore, to elucidate the underlying mechanism for the electric field modulating thermal conductivity, the evolution of charge densities under external electric fields are demonstrated in Fig. 4. On account of the *out-of-plane* mirror asymmetry in Janus monolayer MoSSe structure, spontaneous polarization emerges without any electric field applied, which is indicated by the dipole moment (Fig. 1e) and the dielectric constant (Fig. 1f). With the

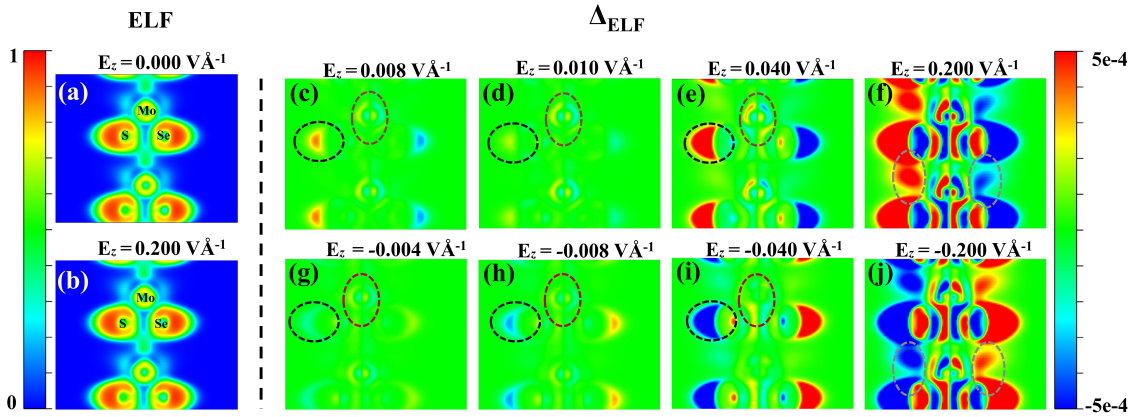

Fig. 5 The comparison of electron localization function (ELF) and the differential ELF (Δ_{ELF}). Detailed ELF of **a** the pristine state and **b** under positive external electric field of 0.2 VÅ^{-1}. **c–j** The differential ELF (Δ_{ELF}) under the typical positive (c-f: 0.008, 0.01, 0.04, 0.2 V Å^{-1}) and negative (**g–j**: −0.004, −0.008, −0.04, −0.2 V Å^{-1}) external electric fields. (Δ_{ELF} = ELF(E_z) − ELF (E_z = 0)). The (−1 2 0) surface is chosen for all the configurations and the isosurface is set as 10^{-5}.

increasing positive electric fields, the renormalization of the charge density around the S, Se, and Mo atoms tends to be gradually noticeable (Fig. 4a–d). However, the renormalization does not occur with negative electric field applied, especially for the Mo atoms. The aggregation of charges around Mo atoms even appears to overturn as the strength of electric field increases (Fig. 4e, h). More detailed information can be found in Supplementary Fig. 6. The charge transfer between Mo and the neighboring S and Se atoms is weakened in the (−1, 2, 0) surface but enhanced for the (2, −1, 0) surface, which becomes dominant subsequently with the increasing negative electric fields. Meanwhile, the differentiation could also be confirmed in Fig. 4d, h (E_z = ±0.200 VÅ^{-1}) as marked by different colored dashed circles (blue, crimson, and gray). In contrast, the different charge responses under reversed electric field leads to different charge redistribution, which results in the asymmetric phonon renormalization and thermal transport behavior (Fig. 2).

Comparison of electron localization function

The electron localization function (ELF) and Δ_{ELF} under the typical electric fields are extracted in Fig. 5 to fundamentally understand the difference in the electronic states with electric fields applied. Generally, the value of ELF ranges from 0 to 1, where a larger value indicates the relatively higher electron occupied states[51]. Here, little difference could be found without and with the positive electric field of 0.2 VÅ^{-1} as shown in Fig. 5a, b, respectively. Thus, the Δ_{ELF} is carried out to further analyse the bonding states, and the result shows that the Δ_{ELF} value of Mo atom demonstrates a generally increasing trend with the increasing strength of the positive electric fields (Fig. 5c–f), while the reversed trends could be found for Mo atoms under negative electric fields (Fig. 5g–i). Note that the variation trend of thermal conductivity is not consistent with the changes of charge densities, which do not continuously increase despite the increasing charge densities. The reason may lie in that the moderate increasing electric field, to some extent, enhances the polarization charge between Mo and S (Se) atoms and future enhances the covalent bond. Consequently, the bond stiffness between Mo and S(Se) atoms is enhanced, resulting in the weakened phonon anharmonicity and enhanced thermal conductivity. Nevertheless, excessive electric field make the charge concentrate extremely close to the Mo, S and Se atoms, which enhances the ionic nature of Mo and S (Se) atoms. Thus, the bond stiffness is weakened and the thermal conductivity is reduced. The competition mechanism resulting from bond stiffness demonstrates the enhanced or weakened polarization of the Mo-S(Se) bonding, which finally leads to the electric field driven increased or decreased thermal conductivities.

Besides, with a reverse electric field applied, the built-in electric field causes a weakened shielding effect with the increasing electric fields, which is caused by the charge distribution transformation from Mo-S(Se) atoms ((−1, 2, 0) surface) to Mo-Mo atoms vacancy ((2, −1, 0) surface). The shielding effect finally leads to the continuously enhanced charge distribution from the S to Se atoms (Fig. 5g–j). The difference in charge distribution leads to the difference in phonon reforming, which finally leads to the difference in thermal transport properties. Generally, the difference mainly originates from the unique Janus structural characteristics, making the difference in the redistributed charge densities when the electric fields are applied in different directions. Such charge density redistribution leads to different phonon renormalization (mainly for the phonon anharmonicity), which eventually leads to the different responses of the thermal conductivity to the external electric fields applied in different directions. Thus, the superior ECTS can be realized based on the electric field driven asymmetric response of the thermal conductivity for Janus MoSSe.

DISCUSSION

In summary, based on *state-of-the-art* first-principles calculations and analysis, we comprehensively investigated the external electric fields modulated thermal transport properties of the Janus monolayers MoSSe. Spontaneous polarization is found due to the absence of mirror symmetry along the *out-of-plane* direction. The asymmetric responses of the thermal conductivities are obtained when the external electric fields are applied in opposite directions, i.e., (anti-)parallel to the *out-of-plane* direction. Interestingly, the results show that the thermal conductivity reaches 2.13 times that of the pristine one under the external electric field of 0.04 V Å^{-1}, which is district from that under the reverse electric fields. Detailed analysis shows that the phonon anharmonicity is responsible for the modulated thermal conductivity under different external electric fields. The changes in charge densities and Δ_{ELF} under electric fields further reveal that it is the redistribution of charge densities that leads to the renormalization of interactions between atoms, which gives rise to phonon reorganization (mainly for the phonon anharmonicity), and finally results in the asymmetric responses of thermal conductivity to external electric fields. Inspiringly, ECTS can be achieved deriving from the differentiated modulation effect by the external electric fields. The more significant realization is that ECTS driven by the gate voltage virtues from the high adjustability, time

efficiency, and stability as well as the convenience of implementation. This study not only expand the selectivity for the design of thermal devices, but also promote the development of nanoelectronic, thermoelectric, and optoelectronic devices. Boldly, we foresee that more two-dimensional materials, especially those with the Janus structures, could be explored for ECTS applications in future.

METHODS

Computational workflow

The DFT calculation is carried out with the Vienna ab-initio simulation package (VASP) with the exchange-correlation functional of Perdew–Burke–Ernzerhof (PBE) of the generalized gradient approximation (GGA)[52,53]. The wave function kinetic energy cutoff is set as the value of 650 eV, which is 2.5 times the maximal pseudo-potentials recommended value. The Hellmann–Feynman force and energy convergence threshold are set 10^{-8} and 10^{-6} eV Å^{-1}, respectively. A Monkhorst–Pack *k*-mesh of 15 × 15 × 1 in the first Brillouin zone (BZ) and a large vacuum spacing of 15 Å along the *out-of-plane* direction is applied for structure optimization[54]. The large vacuum spacing is used to ensure the monolayer structure is not affected by the interaction induced by the periodic boundary conditions between layers. The dipole corrections are taken into consideration during the geometry structure optimization under the different external electric fields along the *out-of-plane* direction.

The thermal conductivity is obtained by solving the phonon Boltzmann transport equation (BTE) implemented in the Sheng BTE package[55]. As the input of the Sheng BTE package, the harmonic interatomic force constants (IFCs) and anharmonic IFCs are extracted by applying the Phonopy[56] and thirdorder.py[55] package, respectively. Here, a 4 × 4 × 1 supercell is constructed and a 2 × 2 × 1 Monkhorst–Pack *k*-mesh is used to sample the BZ. The phonon dispersions are obtained by diagonalizing the harmonic dynamical matrix. Besides, a cutoff radius is introduced during the anharmonic IFCs' calculations to consider the effective atomic interactions. The scattering matrix can be constructed after the anharmonic interatomic force constants are extracted. Subsequently, the phonon scattering information can be obtained. The thermal conductivity is calculated according to the well-known function:

$$k = \sum_{q,v} C_V V_{q,v}^2 \tau_{q,v} \quad (2)$$

where κ donates the lattice thermal conductivity, C_V is the heat capacity depending on phonon frequencies, $V_{q,v}$ is the group velocity of the phonon model with phonon wave vectors q and phonon branches v, which can be calculated by a central difference method, and the $\tau_{q,v}$ is the relaxation time of the corresponding phonon model. For the Janus monolayer MoSSe, the effective thickness is set as 7.0 Å.

DATA AVAILABILITY

The data supporting the findings of this paper are available from the corresponding author upon reasonable request.

Received: 3 September 2022; Accepted: 23 November 2022;
Published online: 24 December 2022

REFERENCES

1. Snyder, G. J. & Snyder, A. H. Figure of merit ZT of a thermoelectric device defined from materials properties. *Energy Environ. Sci.* **10**, 2280–2283 (2017).
2. Poudel, B. et al. High-thermoelectric performance of nanostructured bismuth antimony telluride bulk alloys. *Science* **320**, 634–638 (2008).
3. Maldovan, M. Sound and heat revolutions in phononics. *Nature* **503**, 209–217 (2013).
4. Chaudhry, H. N., Hughes, B. R. & Ghani, S. A. A review of heat pipe systems for heat recovery and renewable energy applications. *Renew. Sustain. Energy Rev.* **16**, 2249–2259 (2012).
5. Rhee, J., Campbell, A., Mariadass, A. & Morhous, B. Temperature stratification from thermal diodes in solar hot water storage tank. *Sol. Energy* **84**, 507–511 (2010).
6. Hao, M., Li, J., Park, S., Moura, S. & Dames, C. Efficient thermal management of Li-ion batteries with a passive interfacial thermal regulator based on a shape memory alloy. *Nat. Energy* **3**, 899–906 (2018).
7. Swanson, T. D. & Birur, G. C. NASA thermal control technologies for robotic spacecraft. *Appl. Therm. Eng.* **23**, 1055–1065 (2003).
8. Wehmeyer, G., Yabuki, T., Monachon, C., Wu, J. & Dames, C. Thermal diodes, regulators, and switches: physical mechanisms and potential applications. *Appl. Phys. Rev.* **4**, 041304 (2017).
9. Kittel, C. & McEuen, P. *Introduction to Solid State Physics*. (John Wiley & Sons, 2018).
10. Liu, H., Zhang, G., Zheng, X., Chen, F. & Duan, H. Emerging miniaturized energy storage devices for microsystem applications: from design to integration. *Int. J. Extrem. Manuf.* **2**, 042001 (2020).
11. Moore, A. L. & Shi, L. Emerging challenges and materials for thermal management of electronics. *Mater. Today* **17**, 163–174 (2014).
12. Liu, H. et al. Ultrathin and ultralight Zn micromesh-induced spatial-selection deposition for flexible high-specific-energy Zn-Ion batteries. *Adv. Funct. Mater.* **16**, 2106550 (2021).
13. Li, N. et al. Colloquium: Phononics: Manipulating heat flow with electronic analogs and beyond. *Rev. Mod. Phys.* **84**, 1045–1066 (2012).
14. Bywaters, R. P. & Griffin, R. A. A gas-gap thermal switch for cryogenic applications. *Cryogenics* **13**, 344–349 (1973).
15. Vanapalli, S., Keijzer, R., Buitelaar, P. & ter Brake, H. J. M. Cryogenic flat-panel gas-gap heat switch. *Cryogenics* **78**, 83–88 (2016).
16. Catarino, I., Afonso, J., Martins, D., Duband, L. & Bonfait, G. Gas gap thermal switches using neon or hydrogen and sorption pump. *Vacuum* **83**, 1270–1273 (2009).
17. Yang, T. et al. Millimeter-scale liquid metal droplet thermal switch. *Appl. Phys. Lett.* **112**, 063505 (2018).
18. Zhu, J. Y., Tang, S. Y., Khoshmanesh, K. & Ghorbani, K. An integrated liquid cooling system based on galinstan liquid metal droplets. *ACS Appl. Mater. Interfaces* **8**, 2173–2180 (2016).
19. Ishibe, T. et al. Tunable thermal switch via order-order transition in liquid crystalline block copolymer. *Nano Lett.* **22**, 6105–6111 (2022).
20. Shrestha, R. et al. High-contrast and reversible polymer thermal regulator by structural phase transition. *Sci. Adv.* **5**, 3777 (2019).
21. Wang, X., Tso, C. Y., Traipattanakul, B. & Chao, C. Y. H. Development of a phase change material (PCM)-based thermal switch. *HKIE Trans.* **24**, 107–112 (2017).
22. Pallecchi, E. et al. A thermal diode and novel implementation in a phase-change material. *Mater. Horiz.* **2**, 125–129 (2014).
23. Ríos, C. et al. Multi-level electro-thermal switching of optical phase-change materials using graphene. *Adv. Photonics Res.* **2**, 2000034 (2021).
24. Cottrill, A. L., Wang, S., Liu, A. T., Wang, W.-J. & Strano, M. S. Dual phase change thermal diodes for enhanced rectification ratios: theory and experiment. *Adv. Energy Mater.* **8**, 1702692 (2018).
25. Lee, S. et al. Anomalously low electronic thermal conductivity in metallic vanadium dioxide. *Science* **355**, 371–374 (2017).
26. Sood, A. et al. An electrochemical thermal transistor. *Nat. Commun.* **9**, 4510 (2018).
27. Du, T. et al. Wide range continuously tunable and fast thermal switching based on compressible graphene composite foams. *Nat. Commun.* **12**, 4915 (2021).
28. Roberts, N. A. & Walker, D. G. A review of thermal rectification observations and models in solid materials. *Int. J. Therm. Sci.* **50**, 648–662 (2011).
29. Adams, M. J., Verosky, M., Zebarjadi, M. & Heremans, J. P. High switching ratio variable-temperature solid-state thermal switch based on thermoelectric effects. *Int. J. Heat. Mass Transf.* **134**, 114–118 (2019).
30. Casati, G., Mejía-Monasterio, C. & Prosen, T. Magnetically induced thermal rectification. *Phys. Rev. Lett.* **98**, 104302 (2007).
31. Jiang, S., Shan, J. & Mak, K. F. Electric-field switching of two-dimensional van der Waals magnets. *Nat. Mater.* **17**, 406–410 (2018).
32. Huang, X. et al. Electric field-induced selective catalysis of single-molecule reaction. *Sci. Adv.* **5**, 3072 (2019).
33. Ihlefeld, J. F. et al. Room-temperature voltage tunable phonon thermal conductivity via reconfigurable interfaces in ferroelectric thin films. *Nano Lett.* **15**, 1791–1795 (2015).
34. Lottermoser, T. et al. Magnetic phase control by an electric field. *Nature* **430**, 541–544 (2004).

35. Zhang, H., Lazo, C., Blügel, S., Heinze, S. & Mokrousov, Y. Electrically tunable quantum anomalous hall effect in graphene decorated by 5*d* transition-metal adatoms. *Phys. Rev. Lett.* **108**, 056802 (2012).
36. He, S., Tian, R., Wu, W., Li, W. D. & Wang, D. Helium-ion-beam nanofabrication: extreme processes and applications. *Int. J. Extrem. Manuf.* **3**, 012001 (2021).
37. Deng, S. et al. Electric-field-induced modulation of thermal conductivity in poly (vinylidene fluoride). *Nano Energy* **82**, 105749 (2021).
38. Deng, S., Ma, D., Zhang, G. & Yang, N. Modulating the thermal conductivity of crystalline nylon by tuning hydrogen bonds through structure poling. *J. Mater. Chem. A* **9**, 24472–24479 (2021).
39. Qin, G., Qin, Z., Yue, S. Y., Yan, Q.-B. & Hu, M. External electric field driving the ultra-low thermal conductivity of silicene. *Nanoscale* **9**, 7227–7234 (2017).
40. Yang, Z., Yuan, K., Meng, J. & Hu, M. Electric field tuned anisotropic to isotropic thermal transport transition in monolayer borophene without altering its atomic structure. *Nanoscale* **12**, 19178–19190 (2020).
41. Traipattanakul, B., Tso, C. Y. & Chao, C. Y. H. A phase-change thermal diode using electrostatic-induced coalescing-jumping droplets. *Int. J. Heat. Mass Transf.* **135**, 294–304 (2019).
42. Miljkovic, N., Preston, D. J., Enright, R. & Wang, E. N. Electrostatic charging of jumping droplets. *Nat. Commun.* **4**, 2517 (2013).
43. Liu, C. et al. Large thermal conductivity switching in ferroelectrics by electric field-triggered crystal symmetry engineering. *ACS Appl. Mater. Interfaces* **3**, 154–166 (2022).
44. Liu, C., Lu, P., Gu, Z., Yang, J. & Chen, Y. Bidirectional tuning of thermal conductivity in ferroelectric materials using E-controlled hysteresis characteristic property. *J. Phys. Chem. C.* **124**, 26144–26152 (2020).
45. Liu, C., Chen, Y. & Dames, C. Electric-field-controlled thermal switch in ferroelectric materials using first-principles calculations and domain-wall engineering. *Phys. Rev. Appl.* **11**, 044002 (2019).
46. Guo, S. D. Phonon transport in Janus monolayer MoSSe: a first-principles study. *Phys. Chem. Chem. Phys.* **20**, 7236–7242 (2018).
47. Dong, L., Lou, J. & Shenoy, V. B. Large In-plane and vertical piezoelectricity in Janus transition metal dichalchogenides. *ACS Nano* **11**, 8242–8248 (2017).
48. Li, F., Wei, W., Zhao, P., Huang, B. & Dai, Y. Electronic and optical properties of pristine and vertical and lateral heterostructures of Janus MoSSe and WSSe. *J. Phys. Chem. Lett.* **8**, 5959–5965 (2017).
49. Zhang, S., Xu, B., Lin, Y., Nan, C. & Liu, W. First-principles study of the layered thermoelectric material TiNBr. *RSC Adv.* **9**, 12886–12894 (2019).
50. Manley, M. E. et al. Intrinsic anharmonic localization in thermoelectric PbSe. *Nat. Commun.* **10**, 1928 (2019).
51. Savin, A., Nesper, R., Wengert, S. & Fässler, T. F. ELF: The Electron localization function. *Angew. Chem., Int. Ed. Engl.* **36**, 1808–1832 (1997).
52. Kresse, G. & Furthmüller, J. Efficient iterative schemes for ab initio total-energy calculations using a plane-wave basis set. *Phys. Rev. B* **54**, 11169–11186 (1996).
53. Perdew, J. P., Burke, K. & Ernzerhof, M. Generalized gradient approximation made simple. *Phys. Rev. Lett.* **77**, 3865–3868 (1996).
54. Monkhorst, H. J. & Pack, J. D. Special points for Brillouin-zone integrations. *Phys. Rev. B* **13**, 5188–5192 (1976).
55. Li, W., Carrete, J., A. Katcho, N. & Mingo, N. ShengBTE: a solver of the Boltzmann transport equation for phonons. *Comput. Phys. Commun.* **185**, 1747–1758 (2014).
56. Togo, A., Oba, F. & Tanaka, I. First-principles calculations of the ferroelastic transition between rutile-type and $CaCl_2$-type SiO_2 at high pressures. *Phys. Rev. B* **78**, 134106 (2008).

ACKNOWLEDGEMENTS

This work is supported by the National Natural Science Foundation of China (Grant Nos. 52006057, 51906097, 11904324, 12274374), the Fundamental Research Funds for the Central Universities (Grant Nos. 531119200237 and 541109010001), the State Key Laboratory of Advanced Design and Manufacturing for Vehicle Body at Hunan University (Grant No. 52175013), and the Natural Science Foundation of Henan Province of China (Grant No. 222300420551). The numerical calculations have been done on the supercomputing system of the E.T. Cluster, the National Supercomputing Center in Changsha, and the Lichtenberg high-performance computer of the TU Darmstadt.

AUTHOR CONTRIBUTIONS

The project was supervised by G.Q. D.W. completed the main investigation, data collection and analysis, and drafted the manuscript. H.W. and Z.Q. initialized the idea of MoSSe and electric field, respectively. C.S., and H.Z. provided great computing resources. E.Z. and J.X. participated in the discussion and assisted correction of the manuscript and figures. All the authors contributed to the final revision of this article.

COMPETING INTERESTS

The authors declare no competing interests.

ADDITIONAL INFORMATION

Supplementary information The online version contains supplementary material available at https://doi.org/10.1038/s41524-022-00944-y.

Correspondence and requests for materials should be addressed to Huimin Wang, Chen Shen, Zhenzhen Qin or Guangzhao Qin.

Reprints and permission information is available at http://www.nature.com/reprints

Publisher's note Springer Nature remains neutral with regard to jurisdictional claims in published maps and institutional affiliations.